## The Role of Cations in the Cation-Driven Assembly Process and their Effect on the Charge Storage Properties of Bilayered Vanadium Oxide and Reduced Graphene Oxide Heterostructures in Alkali Ion Systems

Ryan Andris<sup>1</sup>, Darrell Omo-Lamai<sup>1</sup>, Michael J. Zachman<sup>2</sup>, Ekaterina Pomerantseva<sup>1</sup>\*

**Keywords:** bilayered vanadium oxide; reduced graphene oxide; liquid phase exfoliation; self-assembly; heterostructures; Li-ion batteries; Na-ion batteries

#### **Abstract**

Exfoliated δ-Li<sub>x</sub>V<sub>2</sub>O<sub>5</sub>·nH<sub>2</sub>O (ex-LVO) and reduced graphene oxide (rGO) heterostructures were constructed using different assembling cations (i.e., Li<sup>+</sup>, Na<sup>+</sup>, and K<sup>+</sup> ions). The ex-LVO and rGO nanoflakes were stacked together using a concentrated chloride solution of each assembling cation and vacuum annealed at 200 °C to form three distinct two-dimensional (2D) layered architectures. X-ray diffraction and thermogravimetric analysis confirmed that the assembling ions can control the interlayer spacing of the bilayered vanadium oxide (BVO) phase as well as impact the crystallographic water content, which in turn affects the electrochemical performance. Scanning electron microscopy, scanning transmission electron microscopy (STEM), electron energy-loss spectroscopy (EELS), and X-ray photoelectron spectroscopy confirmed that a 2D heterointerface formed between LVO and rGO, and that the cations used to assemble the heterostructure are trapped in the interlayer BVO region. High-resolution STEM imaging also showed the rGO dispersion throughout the LVO layers. Moreover, STEM-EELS identified a V<sub>2</sub>O<sub>3</sub> phase that forms along the rGO interface that can stabilize the materials during cycling. A charge storage mechanism analysis, combined with galvanostatic intermittent titration technique, found that increased interlayer spacings of the BVO phase and using the assembling cations to define intercalation sites for identical charge carrying ions leads to improved ion diffusion and increased capacities during cycling. Therefore, the Li<sup>+</sup> and Na<sup>+</sup> ion assembled heterostructures showed improved charge carrying ion diffusion and charge storage capacities in each of their respective charge storage systems (i.e., Li-ion and Na-ion half-cells). In total, the cation used for heterostructure assembly can modify the final material structure and tailor the ion diffusion and

<sup>&</sup>lt;sup>1</sup> Department of Materials Science and Engineering, Drexel University, Philadelphia, PA 19104, USA

<sup>&</sup>lt;sup>2</sup> Center for Nanophase Materials Sciences, Oak Ridge National Laboratory, Oak Ridge, TN 37831, USA

<sup>\*</sup> Corresponding Author: ep423@drexel.edu

charge storage capacity to tune its properties for the desired electrochemical system using a variety of 2D materials.

#### 1. Introduction

Lithium-ion battery technology dominates energy storage in portable electronics and electric vehicles because it offers high energy density, high power density, and long-term stability over many cycles<sup>1-4</sup>. However, there is growing interest in beyond Li-ion batteries (e.g., Na-ion and K-ion batteries) due to the natural abundance of Na<sup>+</sup> and K<sup>+</sup> ions, their lower cost, and increased safety<sup>5-9</sup>. In addition, the most studied active materials in these systems do not require elements such as Ni and Co that are becoming increasingly scarce<sup>10, 11</sup>. However, these alternative technologies can be difficult to implement because the current cathode materials do not offer comparative stability, rate capability, or specific capacities to that of their Li-ion counterparts <sup>11-</sup>

Vanadium pentoxide is one promising class of materials for use in Li-, Na-, and K-ion batteries due to its high theoretical capacity and high redox activity  $^{14-16}$ . In particular, the chemically preintercalated bilayered vanadium oxide (BVO or  $\delta$ -M<sub>x</sub>V<sub>2</sub>O<sub>5</sub>·nH<sub>2</sub>O, where M = Li, Na, K, Mg or Ca) phase has been widely studied in these alternative systems because of its tunable interlayer spacing greater than 9 Å that can accommodate larger charge carrying ions and vanadium's ability to undergo multiple reduction steps  $^{17-20}$ . This bilayered phase can also be beneficial because two-dimensional (2D) structures can help enable ion diffusion as well as mitigate structural damage that can occur during extended battery cycling  $^{21}$ . Moreover, there are a variety of strategies that can be implemented to improve the poor electronic conductivity of BVO, including nucleating V<sub>2</sub>O<sub>5</sub> on GO nanosheets, preintercalating small organic molecules into BVO, and incorporating flash-oxidized carbon nanotubes and graphene nanoplatelets during BVO sol-gel synthesis  $^{22-25}$ .

Cation-driven assembly is one promising method that can be used to interface BVO with more conductive two-dimensional (2D) materials. This strategy uses positively charged species to combine one or more 2D phases, often to adjust the final properties of the assembled structure<sup>26-29</sup>. Our recent work used Li<sup>+</sup> ions to assemble exfoliated Li<sub>x</sub>V<sub>2</sub>O<sub>5</sub>·*n*H<sub>2</sub>O (ex-LVO)<sup>30</sup> and monolayer graphene oxide (GO) resulting in the formation of a heterostructure, a 2D material defined by an intimate face-to-face contact between two chemically dissimilar building blocks (structural layers or nanoflakes)<sup>21, 31</sup>. GO was chosen as the conductive carbon precursor because reduced GO (rGO) is an established current collector and conducting agent for the fabrication of electrodes with transition metal oxides<sup>32-34</sup>. This material exhibited enhanced electrochemical

stability and rate capability compared to samples that simply mixed the two components without using cations to initiate this interface formation. Cation-driven assembly has also utilized ions beyond lithium. Alkali metal cations (i.e., Na<sup>+</sup>, K<sup>+</sup>, Rb<sup>+</sup>, Cs<sup>+</sup>, and Ba<sup>2+</sup> ions) were used to assemble exfoliated MoS<sub>2</sub> and WS<sub>2</sub> dichalcogenides in order to incorporate these guest species in their interlayer region<sup>35</sup>. Li<sup>+</sup>, Na<sup>+</sup>, and K<sup>+</sup> ions were also used to flocculate porous MnO<sub>2</sub> nanosheets to form well-ordered manganese oxide layers for supercapacitor applications<sup>27</sup>. A similar report used Li<sup>+</sup>, Na<sup>+</sup>, K<sup>+</sup>, Co<sup>2+</sup>, and Mg<sup>2+</sup> ions to assemble 2D MnO<sub>2</sub> nanosheets with porous frameworks and tunable interlayer spacings dependent on the assembling cation<sup>36</sup>. The study also found that the materials assembled with divalent cations exhibited lower capacities as electrodes in Li-ion and Na-ion batteries compared to the materials assembled with monovalent alkali ions. Moreover, they found that increasing the Na<sup>+</sup> ion/MnO<sub>2</sub> ratio up to 2 optimized the specific capacity in Na-ion batteries by promoting ion diffusion channels, and capacities remained constant beyond this ratio. Therefore, this work builds on previously synthesized LVO and rGO heterostructures to investigate how the assembling cation can affect the structure of the final LVO/rGO materials, and in turn, the electrochemical properties in different charge storage systems using BVO as the active phase.

Herein, Li<sup>+</sup>, Na<sup>+</sup>, and K<sup>+</sup> ions were used to assemble exfoliated Li<sub>x</sub>V<sub>2</sub>O<sub>5</sub>·nH<sub>2</sub>O bilayers and graphene oxide nanoflakes to form 2D heterostructures (**Figure 1**). Na<sup>+</sup> and K<sup>+</sup> ions were utilized in this system for the first time and help demonstrate the versatility of this technique. Further, X-ray diffraction (XRD), thermogravimetric analysis (TGA), and scanning transmission electron microscopy (STEM) demonstrate how changing the assembling cation affects the final structure of the material. In turn, these structures were tested in both Li-ion and Na-ion half-cells for a comprehensive study of how the assembling cation in each structure affects the charge storage mechanism, the diffusion coefficient of the charge carrying ions through the bulk material, and the specific capacity and rate capability of the electrodes. In total, cation-driven assembly can tailor the final structure to obtain properties desirable for specific charge storage systems and is a versatile technique that can be used to interface a variety of 2D materials in aqueous suspensions using any number of positively charged ions.

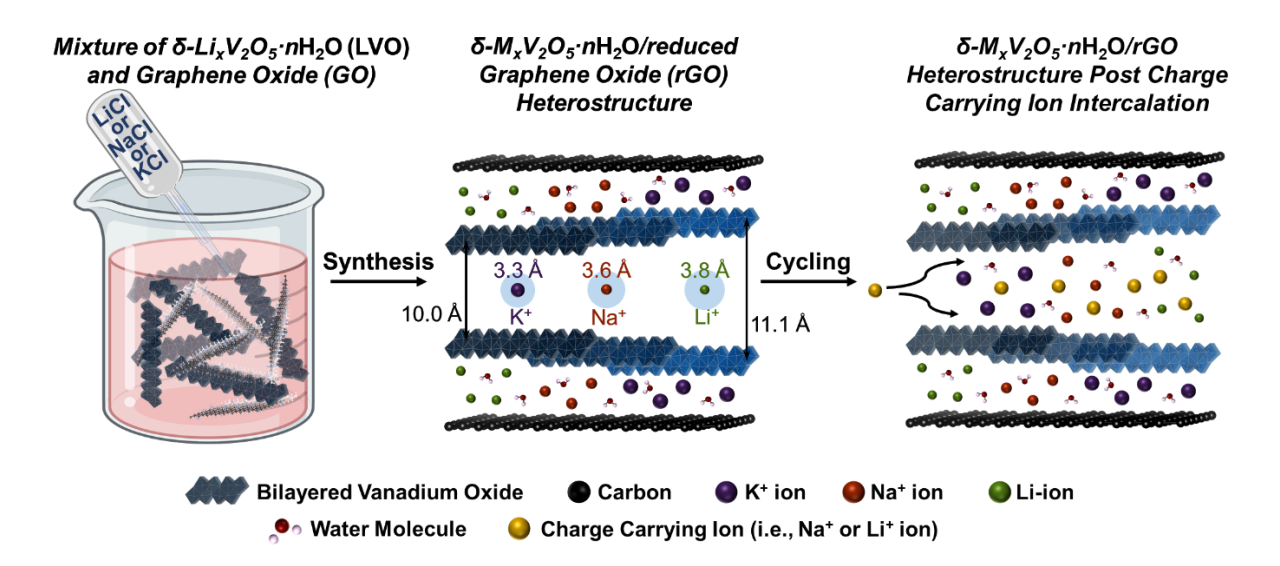


**Figure 1.** Schematic illustration of the heterostructure synthesis process and the range of interlayer spacings that are formed depending on the cation used to assemble the ex-LVO and GO nanoflakes. The initial synthesis step consists of mixing a dispersion of exfoliated  $\delta$ -Li<sub>x</sub>V<sub>2</sub>O<sub>5</sub>·nH<sub>2</sub>O nanoflakes with single-layer GO nanoflakes before slowly adding either 10M LiCl, 5M NaCl, or 4M KCl solution to form the 2D heterostructure via electrostatic interactions. The middle panel is a schematic of the final dehydrated  $\delta$ -M<sub>x</sub>V<sub>2</sub>O<sub>5</sub>·nH<sub>2</sub>O/rGO heterostructure after vacuum filtration and annealing at 200 °C to partially reduce GO and remove crystallographic water, where M can be Li, Na, or K depending on the assembly cation<sup>37</sup>. This schematic also shows the radii of each of these ions in their hydrated form displayed in the central region of the BVO structure with the numbers on the left and ride side indicating the d-spacing that corresponds to the K<sup>+</sup> ion and Li<sup>+</sup> ion assembled samples, respectively. Each of these heterostructures were electrochemically cycled in Li-ion and Na-ion systems as shown in the panel on the right side of the figure.

## 2. Experimental Methods

## Materials Synthesis

Li<sub>x</sub>V<sub>2</sub>O<sub>5</sub>·nH<sub>2</sub>O (LVO) was synthesized using a common sol-gel synthesis method<sup>18, 38</sup>. Briefly, LiCl salt was dissolved in a 15 wt. % hydrogen peroxide solution (Fisher Scientific) to which crystalline α-V<sub>2</sub>O<sub>5</sub> (Acros Organics) powder was slowly added, and a red sol formed and precipitated after several hours. The precipitate was aged for four days, washed with DI water using a vacuum filtration apparatus, and dried at 105 °C in air for 24 hours. The dried material was ground into a powder and dried again at 105 °C for 24 hours. The GO was purchased from Graphenea Inc. in a powder form.

## Exfoliation and Self Assembly

The LVO powder was exfoliated following a previously developed sonication process using a Qsonica Q125 ultrasonic processor with a 3.175 mm diameter probe tip<sup>30</sup>. 225 mg of the powder was added to 10 mL of DI water in a 20 mL vial placed in an ice bath. The suspensions were sonicated for 2 hours at an amplitude of 60%, sonication frequency of 20 kHz, and pulse intervals of 6 seconds on and 2 seconds off. After 1 hour of sonication, the ice bath was replaced. The resulting dispersion was next centrifuged for 10 mins at 10,000 rpm, and the supernatant was collected for the heterostructure assembly. The concentration was determined by drying 1 mL of dispersion in an aluminum boat and weighing the final product after the water evaporated. Separately, the GO powder was suspended in 40 mL of water and bath sonicated at 60 Hz for 30 mins. The ex-LVO dispersion was added to the GO suspension in an 80:20 weight ratio with an additional 40 mL of water and stirred for 5 mins. Next, 5 mL of either 10 M LiCl, 5 M NaCl, or 4 M KCl solution was dropwise added to the mixed ex-LVO/GO suspension over the course of 8 to 10 minutes to induce the cation-driven assembly and allowed to stir for an additional hour. A color change from deep red to red-orange signaled the formation of flocculates. The resulting mixture was centrifuged at 6500 RPM to collect the flocculates and remove the concentrated salt solutions. The flocculates were resuspended in water, washed, and filtered to form a film that was dried at 105 °C. At this stage, the heterostructures are referred to as Li-LVO/GO, Na-LVO/GO, and K-LVO/GO depending on the cation used in the assembly process. Next, the films were ground into a fine powder and annealed at 200 °C under vacuum overnight to obtain rGO and remove excess water<sup>30</sup>. The final prepared heterostructures are referred to as Li-LVO/rGO, Na-LVO/rGO, and K-

LVO/rGO, with rGO indicating that the material was vacuum annealed at 200 °C, or M-LVO/(r)GO in general, where M is either Li, Na, or K.

#### Materials Characterization

The phase composition of the materials during each stage of the synthesis process was determined using a Rigaku benchtop powder X-ray diffraction (XRD) instrument with Cu  $K_{\alpha}$  ( $\lambda =$ 1.54 Å) radiation. XRD patterns were collected using a step size of 0.02° and step speed of 0.7° 20⋅min<sup>-1</sup>. The morphology of the particles was captured using a Thermo Fisher Apreo 2S Lo Vac scanning electron microscope (SEM) equipped with a Trinity detection system and live quantitative energy dispersive X-ray spectroscopy (EDS). SEM images for EDS analysis were acquired using a beam accelerating voltage of 15 kV and an 11 mm working distance (WD). Additionally, samples were sputter coated with a thin ~5 nm layer of Pt/Pd to prevent surface charging and improve image quality. For scanning transmission electron microscopy (STEM) characterization, an electron-transparent cross-sectional sample was produced from a vacuum filtrated film by focused ion beam (FIB) lift-out. Annular dark-field and bright-field STEM imaging, as well as electron energy-loss spectroscopy (EELS) were then performed on an aberration-corrected Nion UltraSTEM 100 operated at 100 kV with a probe semiconvergence angle of ~31 mrad. Images and EELS maps were acquired with doses of <10<sup>4</sup> e<sup>-</sup> Å<sup>-2</sup> and <10<sup>5</sup> e<sup>-</sup> Å<sup>-</sup> <sup>2</sup>, which were sufficiently low to preserve the atomic-scale structure and local bonding environment of the materials. EELS spectrum images were analyzed by multivariate curve resolution (MCR), a statistical analysis method that allows spatially overlapped spectra to be separated into a linear combination of spectral components and their spatial concentrations to be separately mapped. Water and GO contents were evaluated using thermogravimetric analysis (TGA) under ambient air flow using a TA Instruments Q50 by evaluating weight loss from room temperature to 1000 °C using a heating rate of 10 °C·min<sup>-1</sup>. XPS measurements were recorded on a Physical Electronics VersaProbe 5000 using a monochromatic Al Kα source and charge compensation. The high-resolution V 2p and C1s spectra were taken at a pass energy of 23.5 eV with a step size of 0.05 eV. Peak fitting and data analysis were carried out using CasaXPS software. A Shirley background was used for V 2p and C 1s spectra quantification.

#### Electrode and Cell Fabrication

Electrodes were fabricated by first grinding the active material (70 wt. %) and acetylene black (20 wt. %) in a mortar with pestle. Next, this mixture was suspended in poly(vinylidene fluoride) (10 wt. %) and N-methyl-2-pyrrolidone (NMP) to form a viscous slurry using a Flacktek SpeedMixer. The prepared slurry was cast on aluminum foil and dried in a fume hood under room temperature overnight before being placed in an oven at 105 °C for 12 h. 10 mm electrode disks were punched from the dried films. Coin cells were assembled in an argon filled glovebox.

## Electrochemical Testing

All electrochemical data was collected using 2032 type coin cells. The Li-ion system was studied using Li foil as both the counter and reference electrodes, a polypropylene membrane (3501, Celgard USA) served as the separator, and the electrolyte was 1 M LiClO<sub>4</sub> in a 1:1 (v:v) mixture of ethylene carbonate (EC) and dimethyl carbonate (DMC). Na-ion cells were run using metallic Na as the counter and reference electrodes, a glass fiber separator, and a 1M NaClO<sub>4</sub> in a 1:1 (v:v) EC and propylene carbonate (PC) electrolyte. Each cell was cycled in a 2 – 4 V window. Cyclic voltammograms (CVs) were collected using a BioLogic VP3 potentiostat at sweep rates of 0.1, 0.2, 0.4, 0.6, and 0.8 mV s<sup>-1</sup>. Galvanostatic cycling experiments were run at a 20 mA·g<sup>-1</sup> specific current on an Arbin battery testing station. Lastly, rate capability experiments were conducted for 10 cycles each at specific currents of 20 mA g<sup>-1</sup>, 50 mA g<sup>-1</sup>, 100 mA g<sup>-1</sup>, 200 mA g<sup>-1</sup>, and 20 mA g<sup>-1</sup>.

#### 3. Results and Discussion

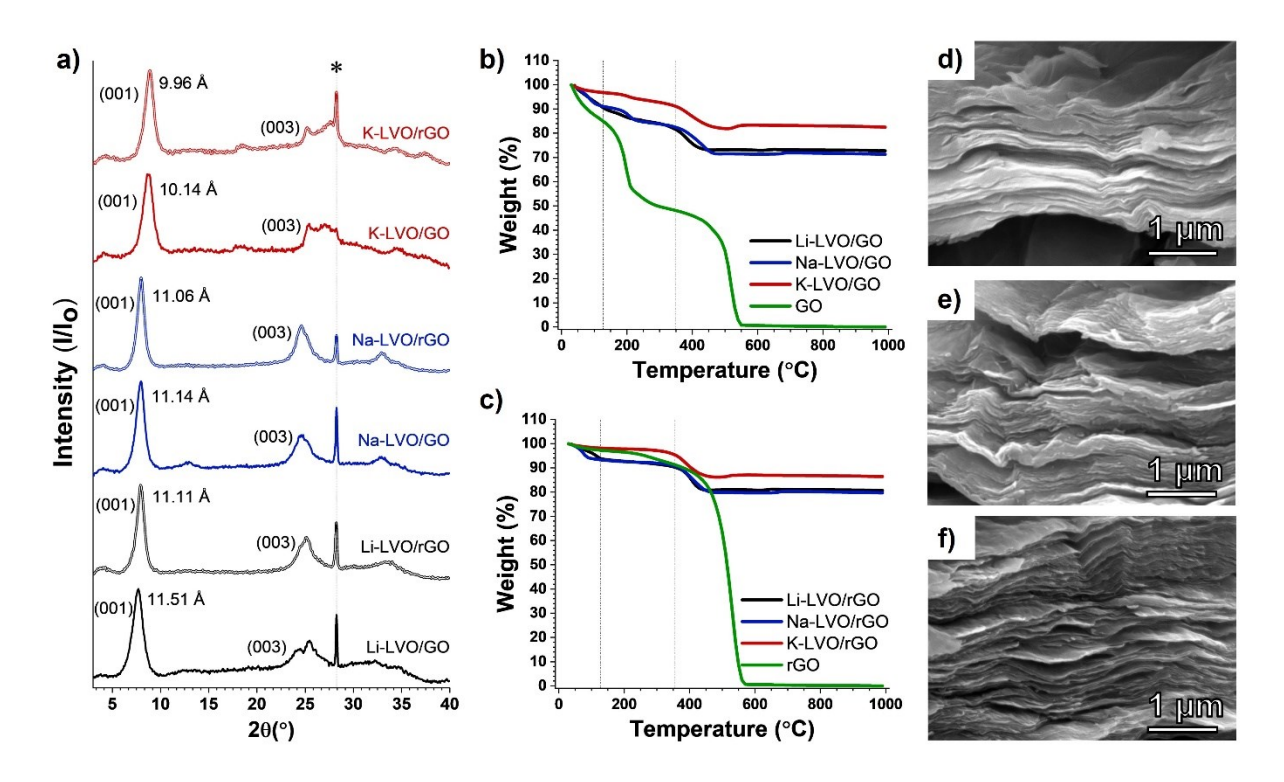


**Figure 2.** Characterization of the 2D heterostructures. (a) XRD patterns of the M-LVO/(r)GO heterostructures before and after annealing, signified by the single and double lines, respectively. The dotted line at approximately 28° 2θ is the Si reference. (b,c) TGA weight loss curves of the assembled M-LVO/(r)GO heterostructures and (r)GO reference (b) before and (c) after annealing at 200 °C under vacuum. (d-f) SEM images of Li-LVO/rGO, Na-LVO/rGO, and K-LVO/rGO heterostructures, respectively, taken using an in-lens detector.

Each LVO/GO structure used either Li<sup>+</sup>, Na<sup>+</sup>, or K<sup>+</sup> ions to assemble negatively charged exfoliated bilayered vanadium oxide and GO nanoflakes to form a layered 2D heterostructure. In order to improve the electronic conductivity of the GO phase and reduce the amount of water present in the LVO bilayers, each material was annealed at 200 °C under vacuum to form reduced GO (rGO)<sup>30, 39, 40</sup>. As shown in a previously published report using this cation-driven assembly method<sup>31</sup>, each XRD pattern exhibits (00*l*) peak reflections characteristic of the δ-V<sub>2</sub>O<sub>5</sub>·*n*H<sub>2</sub>O phase (**Figure 2a**)<sup>17</sup>. The (001) peaks of the Li-LVO/rGO, Na-LVO/rGO, and K-LVO/rGO heterostructure spectra prior to annealing are located at ~7.68°, ~7.93°, and ~8.71° 2θ, respectively, which correspond to *d*-spacings of ~11.51, ~11.14, and ~10.14 Å. These interlayer distances were calculated using Bragg's law and are shown next to their respective (001) peaks.

After annealing, these d-spacings were reduced to ~11.11, ~11.06, and ~9.96 Å (i.e., located at ~7.95°, ~7.98°, and 8.87° 20), respectively. This reduction in interlayer spacing could be due to a loss of crystallographic water in the bilayered structure during vacuum annealing<sup>31</sup>. In addition, these values are in good agreement with previously reported Li<sup>+</sup>, Na<sup>+</sup>, and K<sup>+</sup> ion preintercalated bilayered vanadium oxide phases<sup>18, 41</sup>. This result supports the hypothesis that the cations used during assembly are trapped between the LVO/rGO layers and define the interlayer spacing of the structure in proportion to the hydrated radius of the respective cation. Therefore, cation-driven assembly produces similar results to that of the chemical preintercalation method in terms of defining the chemical composition and structure. The chemical preintercalation method and the cation-driven assembly strategy can be thought of as 'bottom-up' and 'top-down' synthesis approaches, respectively.

The TGA curves presented in Figure 2b and 2c help show the successful removal of interlayer water and the reduction of the GO nanoflakes. Each structure is comprised of weakly bound surface water, (r)GO nanoflakes, double-layered M<sub>x</sub>V<sub>2</sub>O<sub>5</sub>, and the structural water present within the M<sub>x</sub>V<sub>2</sub>O<sub>5</sub> interlayer region. The weakly bound physiosorbed water is removed via evaporation at temperatures below 110 °C. Of note, the K-LVO/(r)GO material exhibits ~70% less weight loss in this region compared to heterostructures assembled with Li<sup>+</sup> and Na<sup>+</sup> ions both before and after annealing. This result is consistent with previously published K<sup>+</sup> ion intercalated δ-V<sub>2</sub>O<sub>5</sub>·nH<sub>2</sub>O materials that measured low surface water content, and suggests these materials have a low affinity for water<sup>41-43</sup>. The oxygen containing functional groups present in GO are typically removed between 150 °C and 350 °C<sup>40, 44, 45</sup>. Prior to annealing, the inflection points in the TGA curves of the heterostructures at ~165 °C and the GO reference at ~150 °C delineate the removal of these groups<sup>31</sup>. Simultaneously, the  $\delta$ -M<sub>x</sub>V<sub>2</sub>O<sub>5</sub>·nH<sub>2</sub>O structural water is lost between 110 °C and 400 °C, as evidenced by the sloping weight loss curves in this temperature region<sup>20, 46</sup>. After annealing, the slope of the TGA curves in this region is noticeably reduced, which indicates that some of the structural water was removed and rGO was formed. The sp<sup>2</sup> hybridized graphene component of each heterostructure and rGO reference sample subsequently combusts at temperatures above ~ 350 °C<sup>31</sup>. Lastly, weight gain observed above ~ 450°C can be attributed to the filling of oxygen vacancies present in the V<sub>2</sub>O<sub>5</sub> layers<sup>41, 47, 48</sup>.

The TGA curves can also be used to estimate the molar mass of the heterostructures after annealing. Calculating the structural water and final carbon content of the heterostructures is challenging due to the simultaneous removal of this water content and combustion of rGO. However, these values can be estimated by normalizing each TGA curve by the mass left after the removal of physiosorbed water, calculating the weight loss between ~110 and ~350 °C assuming it can be attributed to the removal of structural water, as well as measuring the weight loss that occurs above ~350 °C due to the combustion of sp² hybridized carbon. This method estimates that the Li-LVO/rGO, Na-LVO/rGO, and K-LVO/rGO samples are comprised of 2.1, 1.4, and 1.2 wt. % crystallographic water and 11.2, 12.8, and 11.2 wt.% rGO, respectively. In turn, the molar mass of each respective material is ~209.9, ~212.1, and ~207.7 g mol<sup>-1</sup>. The consistent carbon content across each sample supports the reproducibility of the cation-driven assembly method.

While an (r)GO signal does not appear in the XRD spectra due to the irregular dispersal of these nanoflakes throughout the heterostructure, both SEM and STEM imaging show the presence of rGO nanoflakes interspersed with ex-LVO. The cross-sectional SEM images in Figure 2, d-f and the higher magnification images in Figure S1, a-c (Supporting Information) show the stacked 2D morphology of the cation-assembled materials. The regions captured in these images were used in combination with EDS mapping to help show the layering of the ex-LVO and rGO components on a micron scale, also shown in Figure S1. However, while the carbon signal does show evidence of these layers, the vanadium signal is more uniform compared to our previous cation-assembled heterostructures<sup>31</sup>. This outcome could be due to improved synthesis processing that resulted in a better distribution of vanadium oxide and carbon layers and more uniform elemental maps. Therefore, STEM imaging is required to confirm there is a 2D interface between LVO and rGO nanoflakes. In contrast, both the EDS maps and spectra were effective in showing the presence of a Na<sup>+</sup> and K<sup>+</sup> ion signal in the Na-LVO/rGO and K-LVO/rGO structures, respectively (Figure S2 in Supporting Information). This data supports the idea that these ions are captured between the nanoflakes during cation-driven assembly.

To better understand the ex-LVO and rGO nanoflake distribution and interface formation, higher resolution STEM imaging and EELS were employed. Annular dark-field (ADF)-STEM imaging revealed the presence of heterostructures consisting of nm-scale rGO layers between LVO layers that ranged approximately from one to tens of nm thick (**Figure 3**). In general, the Li-

LVO/rGO and Na-LVO/rGO samples had clearly dispersed rGO layers, while the rGO layers in the K-LVO/rGO sample appear denser in the localized imaging. In addition, EELS revealed two separate V and O local bonding environments in the samples, consistent with V<sub>2</sub>O<sub>5</sub> and V<sub>2</sub>O<sub>3</sub><sup>49</sup>. The majority of the LVO material consisted of V<sub>2</sub>O<sub>5</sub> for the Li-LVO/rGO and Na-LVO/rGO samples, with approximately 2-3 nm thick V<sub>2</sub>O<sub>3</sub> layers present at the LVO-rGO interfaces. Low-loss EELS further supported the presence of these interfacial layers (**Figure S3** in **Supporting Information**). The V<sub>2</sub>O<sub>3</sub> was more widespread in the K-LVO/rGO sample, likely due to the increased density of rGO layers, and therefore, rGO-LVO interfaces. Finally, low-loss and coreloss EELS also confirmed the presence of Li and K in the Li-LVO/rGO and K-LVO/rGO samples, respectively (**Figure S3** in **Supporting Information**).

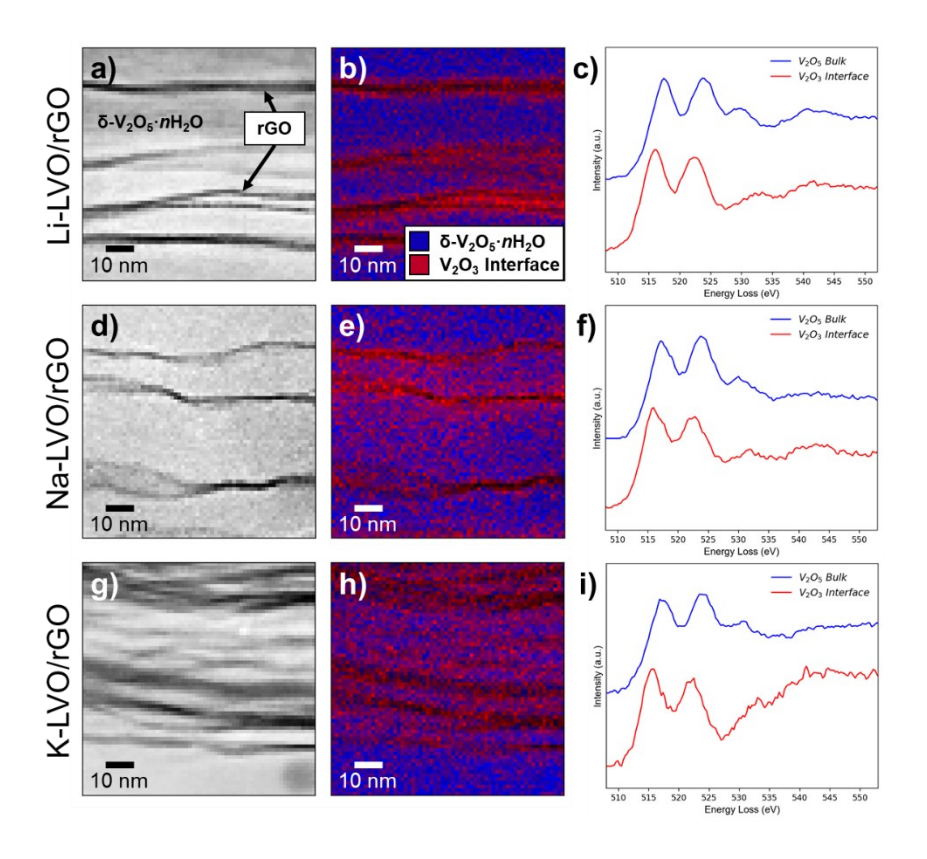


**Figure 3.** High-resolution STEM and EELS characterization of M-LVO/rGO heterostructures. Analysis of (a-c) Li-LVO/rGO, (d-f) Na-LVO/rGO, and (g-i) K-LVO/rGO heterostructures using simultaneously acquired (a, d, g) ADF-STEM images, (b, e, h) EELS maps, and (c, f, i) corresponding V L-edge and O K-edge spectra separated and mapped by multivariate curve resolution. The well-separated nature of the heterostructures in the Li-LVO/rGO and Na-LVO/rGO samples enabled approximately 2-3 nm thick V<sub>2</sub>O<sub>3</sub> layers to be observed at the LVO-rGO interfaces. The V<sub>2</sub>O<sub>3</sub> signal was less localized in the K-LVO/rGO case, likely due to the density of rGO layers present.

Analysis of the XPS spectra helps confirm the presence of the assembling cations within the structure, the reduction of the GO nanoflakes, and the high oxidation state of vanadium in the bulk structure. The survey scans of the Na-LVO/rGO and K-LVO/rGO heterostructures show peaks corresponding to the Na 1s and K 2p binding energies, respectively (Figure S4 in Supporting Information). These peaks are in agreement with Na-LVO/rGO and K-LVO/rGO cross-sectional EDS spectra that show a Na<sup>+</sup> and K<sup>+</sup> ion signal, respectively, as well as the K-LVO/rGO EELS spectrum that displays a K L-edge and the Li-LVO/rGO EELS spectrum that shows a Li K-edge (Figure S3 in Supporting Information). Together, these characterization methods verify these ions are captured by the nanoflakes during the assembly process. In addition, the C1s spectra in Figure S5 in the Supporting Information show a reduction in the areas corresponding to C - O and C = O bonds relative to the  $sp^2$  and  $sp^3$  hybridized carbon bonds, confirming the reduction of the GO nanoflakes in each heterostructure after vacuum annealing at 200 °C. Moreover, while localized STEM analysis found variable amounts of the V<sub>2</sub>O<sub>3</sub> phase concentrated along the rGO interface, the V 2p spectra in Figure S6 in the Supporting **Information** confirm that vanadium maintains a mixed V<sup>5+</sup>/V<sup>4+</sup> oxidation state after annealing in the bulk material (i.e., average vanadium oxidations states of 4.88, 4.83, and 4.86 for the Li-LVO/rGO, Na-LVO/rGO, and K-LVO/rGO heterostructures, respectively). A summary of the contributions of the functional groups present in the C1s spectra and vanadium oxidation states are shown in Table S1 in Supporting Information, and a more detailed analysis of the XPS spectra can be found in a previous publication<sup>31</sup>.

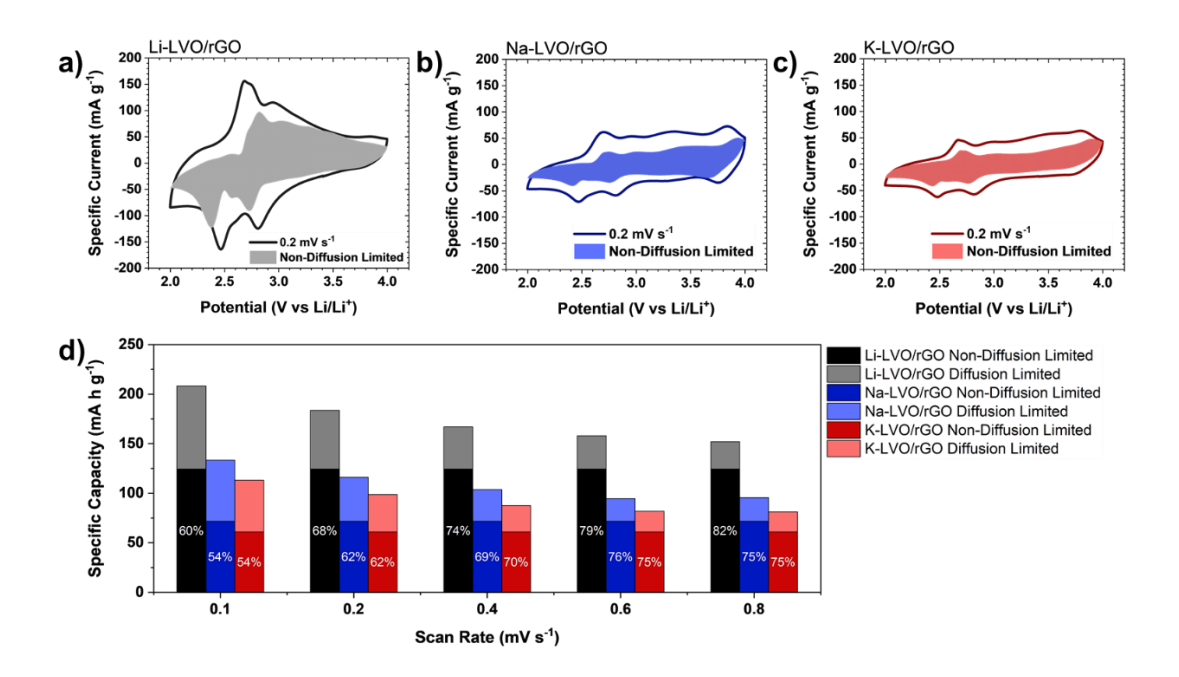


**Figure 4.** Charge storage mechanism analysis in Li-ion half-cells. (a) Black Li-LVO/rGO, (b) blue Na-LVO/rGO, and (c) green K-LVO/rGO electrode CV curves showing the total charge storage and non-diffusion limited charge storage contributions obtained at a 0.2 mV s<sup>-1</sup> scan rate denoted by the solid line and shaded regions, respectively. (d) A summary of the diffusion limited and non-diffusion limited charge storage contributions of each heterostructure at increasing scan rates using the same color coding marked by the lighter shade and darker shade, respectively. The percentages denote the amount of non-diffusion charge storage contribution for each heterostructure at each scan rate.

To study the effect the assembling cation has on the charge storage properties of the heterostructures, each material was initially evaluated using cyclic voltammetry in Li-ion half cells. The Li-LVO/rGO, Na-LVO/rGO, and K-LVO/rGO CV curves captured using a 0.2 mV s<sup>-1</sup> sweep rate (**Figure 4, a-c**) exhibit similar features owing to the bilayered vanadium oxide serving as the active phase in each structure. There is a prominent anodic peak at 2.7 V, a more subtle anodic peak at 2.95 V, and their corresponding cathodic peaks at 2.45 V and 2.8 V vs Li/Li<sup>+</sup> that show the reversible ion intercalation-type behavior of this system. In addition, the galvanostatic discharge charge (GDC) profiles of the first two cycles are shown in **Figure S7a-c** in the **Supporting Information.** Both the peaks and plateaus are consistent with previous electrochemical studies of bilayered vanadium oxides behavior<sup>24, 30, 31, 41</sup>. However, the Li-LVO/rGO curve exhibits increased specific currents of the peaks associated with redox processes

at each of these potentials. This result suggests that the Li<sup>+</sup> ions used to assemble this sample could help define intercalation sites for charge carrying Li<sup>+</sup> ions and facilitate the transport of Li<sup>+</sup> ions at these potentials. Therefore, we performed a more detailed analysis of the charge storage mechanism of each material.

The current response at discrete voltage steps in each curve can be attributed to diffusion limited and non-diffusion limited charge storage mechanisms as described using equation 1:

$$i(V) = k_1 v + k_2 v^{1/2} (1)$$

Where *i* is the measured current, *v* is the voltage sweep rate,  $k_1v$  is the non-diffusion limited current contribution, and  $k_2v^{1/2}$  is the diffusion limited current contribution<sup>50</sup>. The  $k_1$  and  $k_2$  values are determined analytically with equation 2 using the measured current of CV curves obtained at increasing voltage sweep rates (**Figure S8** in **Supporting Information**).

$$i(V)/v^{1/2} = k_1 v^{1/2} + k_2 (2)$$

This analysis helped elucidate several key observations in the Li-ion charge storage system. As can be seen in **Figure 4d** and **Table S2** in **Supporting Information**, the overall capacity of each heterostructure electrode shrinks as the scan rate increases. This result is expected because the amount of time available for Li<sup>+</sup> ions to diffuse into the structures is reduced. **Figure 4d** also shows that the Li-LVO/rGO electrode has the highest relative contribution from non-diffusion limited charge storage at each scan rate. Moreover, the Li<sup>+</sup> ion assembled structure has the highest absolute capacity from both diffusion limited and non-diffusion limited charge storage mechanisms, as summarized in **Table S2**. As the interlayer spacings decrease with the Na<sup>+</sup> and K<sup>+</sup> ion assembled structures, the overall capacity is reduced and there is a relative decrease in diffusion limited charge storage. This result suggests that the increased interlayer spacing and the potential for assembling Li<sup>+</sup> ions to define charge storage sites in the Li-LVO/rGO heterostructure when cycled in Li-ion half cells results in facilitated Li<sup>+</sup> ion diffusion during cycling, leading to higher diffusion-limited and non-diffusion charge storage capacities.

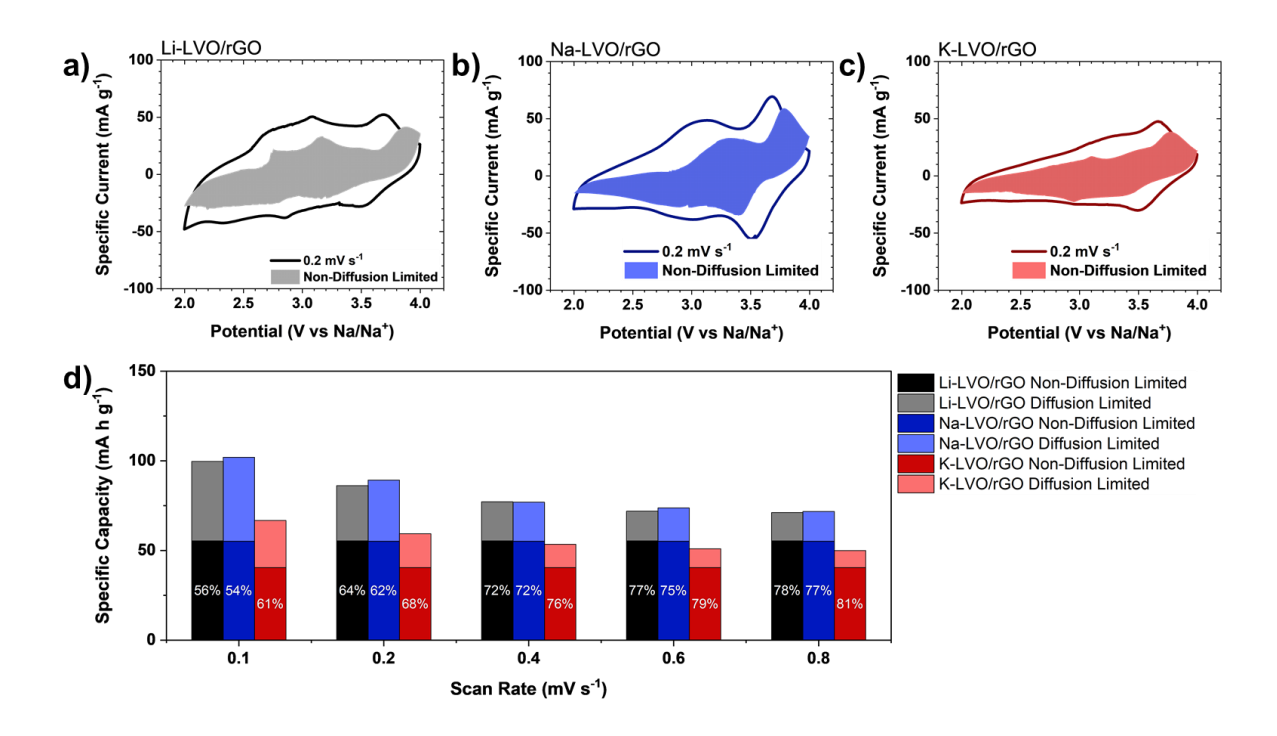


**Figure 5.** Charge storage mechanism analysis in Na-ion half-cells. (a) Black Li-LVO/rGO, (b) blue Na-LVO/rGO, and (c) green K-LVO/rGO electrode CV curves showing the total charge storage and non-diffusion limited charge storage contributions obtained at a 0.2 mV s<sup>-1</sup> scan rate denoted by the solid line and shaded regions, respectively. (d) A summary of the diffusion limited and non-diffusion limited charge storage contributions of each heterostructure at increasing scan rates using the same color coding marked by the lighter shade and darker shade, respectively. The percentages denote the amount of non-diffusion charge storage contribution for each heterostructure at each scan rate.

The same charge storage mechanism analysis was completed for each heterostructure in a Na-ion system using the CV curves found in **Figure S9** in the **Supporting Information**. Again, there are similarities in each of the heterostructure CV curves, with the strongest corresponding anodic and cathodic peaks at 3.65 and 3.5 V, respectively. However, there is a broader anodic and cathodic couplet centered at 3.1 and 3.0 V for the Na-LVO/rGO sample curve whereas the K-LVO/rGO electrode exhibits a more rectangular CV curve at lower potentials. While the Li-LVO/rGO electrode CV curve does appear to have small corresponding peaks at 3.1 and 2.85 V, they are less distinct than in the Na<sup>+</sup> ion assembled sample curve. Overall, this outcome contrasts with the Li-ion system, where the CV curves show that a higher proportion of the total specific capacity is due to redox reactions at lower potentials. This behavior can also be seen in the GDC

profiles shown in **Figure S7d-f** in the **Supporting Information**. Of note, a previous report that cycled BVO in both Li-ion and Na-ion cells also found that a higher fraction of charge is stored at potentials greater than ~2.75 V vs Na<sup>+</sup>/Na in the Na-ion system compared to the Li-ion system<sup>20</sup>. Moreover, the Na<sup>+</sup> ion assembled sample CV curve exhibits the highest anodic and cathodic specific current peaks at 3.65 and 3.5 V in the Na-ion system, a similar trend to that shown by the Li<sup>+</sup> ion assembled sample CV curve in the Li-ion system.

The Na-LVO/rGO electrode shows the highest overall capacity compared to both the Li-LVO/rGO and K-LVO/rGO samples in Na-ion half cells (Figure 5d). However, the Na-LVO/rGO electrode generally has lower non-diffusion limited charge storage contributions to its capacity compared to the Li-LVO/rGO electrode at each scan rate (Table S3 in the Supporting **Information**). For example, the Na<sup>+</sup> ion assembled electrode has non-diffusion limited charge storage contributions of 54% and 77% at 0.1 and 0.8 mV s<sup>-1</sup> scan rates while the Li<sup>+</sup> ion assembled electrode exhibits non-diffusion limited charge storage contributions of 56% and 78% at the same scan rates. This result implies that more charge carrying Na<sup>+</sup> ions are diffusing into the Na<sup>+</sup> ion assembled heterostructure. Therefore, there are at least two primary competing factors in the cation-driven assembly system. Both the interlayer spacing of the vanadium bilayers and the cation used to assemble the 2D structure seem to affect the diffusion of the charge carrying ion. The Li<sup>+</sup> ion assembled sample has the largest interlayer spacing, which leads to improved non-diffusion limited charge storage and the highest capacity in the Li-ion system. In contrast, the K-LVO/rGO heterostructure that has both the smallest interlayer spacing and charge storage capacity, a trend observed in a report that used cation-driven assembly to stack MnO<sub>2</sub> nanosheets<sup>36</sup>. Moreover, the assembling cation also seems to facilitate diffusion when this cation is identical to the charge carrying ion (i.e., the Na-LVO/rGO sample has the largest diffusion limited capacity in the Na-ion system). Therefore, the galvanostatic intermittent titration technique (GITT) was used for a more in-depth analysis of the diffusive properties of both the Na-ion and Li-ion systems.

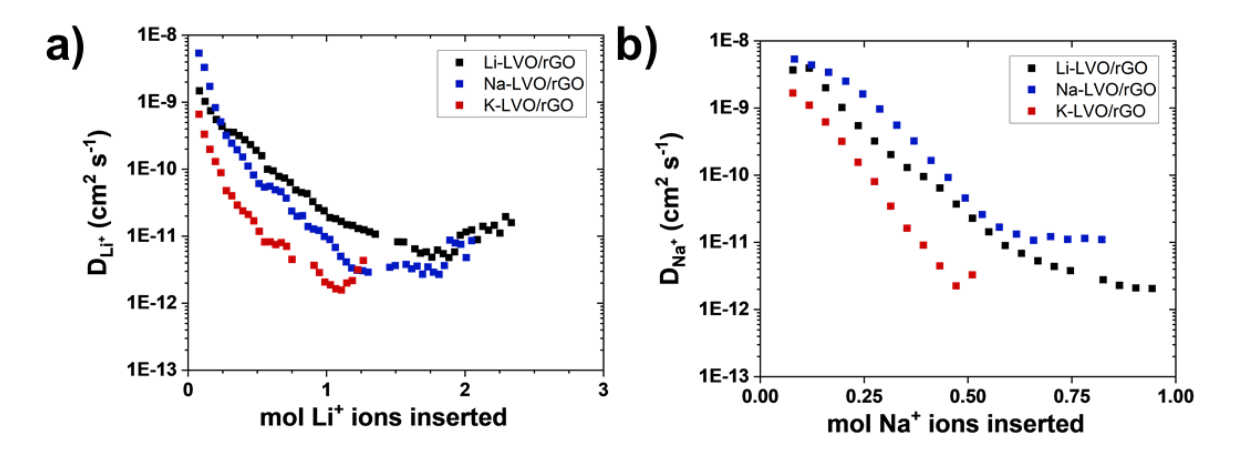


**Figure 6.** Experimentally obtained diffusion coefficients of charge carrying ions. (a) Li<sup>+</sup> ion and (b) Na<sup>+</sup> ion diffusion coefficients measured in Li-ion and Na-ion systems, respectively, for each Li-LVO/rGO, Na-LVO/rGO, and K-LVO/rGO heterostructure. The diffusion coefficients were calculated using **Equation 3** with key variables obtained using the processes outlined in **Figure S10** and **Figure S11** for the Li-ion and Na-ion systems, respectively.

GITT experiments consisted of 30 min of applied negative specific current at 10 mA g<sup>-1</sup> followed by 20 hours of rest at open circuit. This sequence was repeated in the same 2-4 V potential window as the galvanostatic and potentiostatic cycling experiments. The Li<sup>+</sup> and Na<sup>+</sup> ion apparent diffusion coefficients, denoted as  $D_{Li}^+$  and  $D_{Na}^+$ , respectively, were calculated for each material in each cycling system using **Equation 3**:

$$D = \frac{4}{\pi} \left(\frac{m_B V_m}{M_B S}\right)^2 \left[\frac{\left(\frac{\Delta E_{eq}}{\Delta t_I}\right)}{\tau\left(\frac{dE}{d\sqrt{t}}\right)}\right]^2 \tag{3}$$

Where  $m_B$ ,  $V_m$ ,  $M_B$ , S, and  $\tau$ , are the active mass, molar volume, molar mass, the interfacial area between the electrolyte and electrode of the heterostructure materials, and the constant current pulse time, respectively. For the purpose of this study, S was taken as the geometric area of the electrode.  $\Delta E_{eq} / \Delta t_I$  is the change in the equilibrium voltage that occurs due to the change in the electrode's stoichiometry during the current on period, illustrated in **Figure S10b** and **Figure S11b** in **Supporting Information**. This term can be taken simply as the difference in equilibrium voltages assuming sufficiently low current is applied for short durations. Finally,  $dV/d\sqrt{t}$  is the slope of the linear region of the potential against the square root of time duration during the period of applied current as shown in **Figure S10c** and **Figure S11c** in **Supporting Information**<sup>51</sup>.

As suggested during the discussion of the charge storage mechanism, there are clear trends that can be identified in both the Li-ion and Na-ion systems shown in Figure 6. When cycled in a Li-ion half-cell, the Li<sup>+</sup> ion assembled sample demonstrates consistently improved D<sub>Li</sub><sup>+</sup> values when compared to the Na<sup>+</sup> and K<sup>+</sup> ion assembled materials (Figure 6a). Most notably, at approximately 1 M of Li<sup>+</sup> ions inserted, the Li-LVO/rGO heterostructure has an estimated D<sub>Li</sub><sup>+</sup> twice that of the Na-LVO/rGO heterostructure and a full two orders of magnitude higher than the K-LVO/rGO heterostructure. The increase in  $D_{Li}^+$  observed at the tail end of each of the sample plots was observed in a previous report and could be attributed to electrochemically induced fracture that can provide fast ion transport paths<sup>52</sup>. In contrast, the Na-LVO/rGO sample shows the highest  $D_{Na}^+$  values in the Na-ion system (**Figure 6b**) while the K<sup>+</sup> assembled sample maintains the lowest measured diffusion coefficients. These results in the Na-ion system agree with trends found previously for templated tunnel manganese oxides<sup>53</sup>. The poor ion diffusion observed in the K-LVO/rGO heterostructure could partially be attributed to the K<sup>+</sup> ions used for assembly occupying a more central region of the interlayer gallery, thereby hindering ion intercalation, a phenomenon measured in a Ti<sub>3</sub>C<sub>2</sub> MXene material<sup>54</sup>. Of note, the Na<sup>+</sup> assembled sample exhibits higher average  $D_{Na}^+$  values compared to  $D_{Li}^+$  values (i.e.,  $1.03E^{-9}$  cm<sup>2</sup> s<sup>-1</sup> compared to  $2.5E^{-10}$  cm<sup>2</sup>  $s^{-1}$ ). The same trend is observed when comparing  $D_{Li}^{+}$  and  $D_{Na}^{+}$  of the  $Li^{+}$  ion assembled sample (i.e., 1.36E<sup>-10</sup> cm<sup>2</sup> s<sup>-1</sup> compared to 5.51E<sup>-10</sup> cm<sup>2</sup> s<sup>-1</sup>). These results further support the idea that a combination of larger interlayer spacings and assembling ions that can define preintercalation sites for identical charge carrying ions result in better electrochemical charge storage properties.

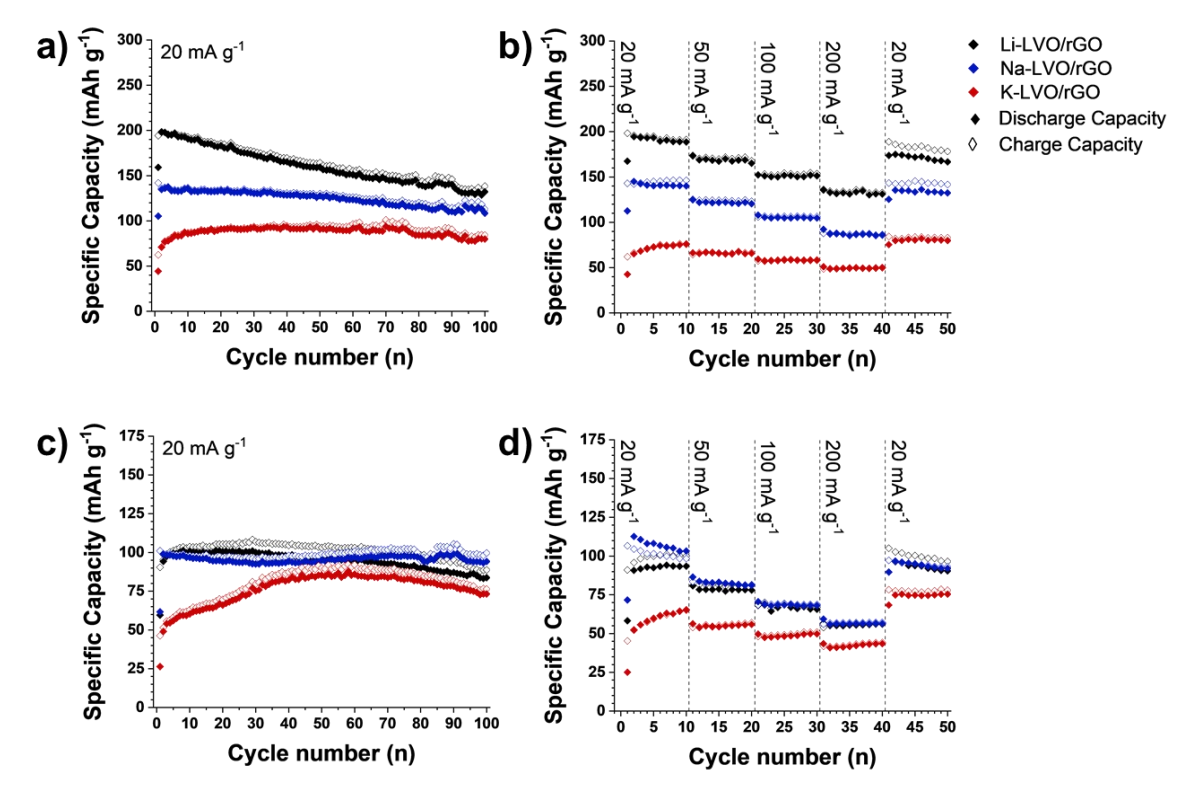


**Figure 7.** Galvanostatic testing in Na-ion and Li-ion cells. (a,c) Life cycle testing and (b,d) rate performance data of Li-ion and Na-ion half cells, respectively, containing Li-LVO/rGO, Na-LVO/rGO, and K-LVO/rGO heterostructure electrodes.

Each of the heterostructures were also tested for long-term cycling stability and rate performance in Li-ion and Na-ion half-cells (**Figure 7**). As stated previously, the Li<sup>+</sup> ion assembled material exhibits the highest capacity in the Li-ion system (195 mAh g<sup>-1</sup>) compared to the Na<sup>+</sup> ion assembled material (136 mAh g<sup>-1</sup>) and the K<sup>+</sup> ion assembled material (80 mAh g<sup>-1</sup>). In addition, the Li-LVO/rGO electrode retained the highest amount of its initial capacity when increasing the specific current from 20 mA g<sup>-1</sup> to 200 mA g<sup>-1</sup> relative to the Na-LVO/rGO and K-LVO/rGO electrodes during the rate capability study (i.e., 70%, 62%, and 66% respectively). However, it preserved only ~91% of its initial capacity after the current returned to 20 mA g<sup>-1</sup> compared to ~94% for the Na-LVO/rGO material and ~100% for the K-LVO/rGO structure. In addition, after 100 cycles at a 20 mA g<sup>-1</sup> specific current, the Li-LVO/rGO heterostructure demonstrated a specific discharge capacity of only 132 mA g<sup>-1</sup>, a capacity retention of 68%, while the Na<sup>+</sup> and K<sup>+</sup> ion assembled samples showed 80% and 100% capacity retention after 100 cycles (i.e., 109 and 80 mAh g<sup>-1</sup>, respectively). The reduced electrochemical stability may be related to the increased

crystallographic water present in the Li-LVO/rGO sample which has been shown to lead to capacity fade<sup>55</sup>. The performance of this heterostructure could potentially be improved by using a divalent cation such as the  $Mg^{2+}$  ion. BVO preintercalated with  $Mg^{2+}$  ions maintains a large interlayer spacing<sup>18, 41</sup>, which can be important for charge storage properties as demonstrated in this work. Moreover, a recent publication that used cations to assemble  $\alpha$ -V<sub>2</sub>O<sub>5</sub> and rGO found that assembling cations with higher oxidation states acted as more stable pillars to support the V<sub>2</sub>O<sub>5</sub> layers and the interface between V<sub>2</sub>O<sub>5</sub> and rGO<sup>56</sup>.

In the Na-ion system, the Na-LVO/rGO heterostructure showed the highest initial capacity of 99 mAh g<sup>-1</sup> compared to the 94 and 49 mAh g<sup>-1</sup> capacities shown by the Li-LVO/rGO and K-LVO/rGO structures. It also showed an impressive 95% capacity retention (94 mAh g<sup>-1</sup> capacity) after 100 discharge charge cycles compared to the 84% retention observed for the Li<sup>+</sup> ion assembled material. Interestingly, the K-LVO/rGO heterostructure shows clear activation behavior in the Na-ion system. This phenomenon is likely related to the relatively small interlayer spacing of this sample in addition to the K<sup>+</sup> ions occupying a more central region between the BVO bilayers, thereby impeding Na-ion electrolyte penetration into the K-LVO/rGO heterostructure<sup>54</sup>. Moreover, the relatively lower capacities exhibited by this material in the Li-ion and Na-ion systems could also be related to the increased proportion of the V<sub>2</sub>O<sub>3</sub> phase found along the rGO interface in STEM analysis in combination with the lower interlayer spacing. However, this same interface combined with the lower water content may play a strong role in the electrochemical stability exhibited by the K-LVO/rGO heterostructure. As far as the rate performance in the Naion system, the Li<sup>+</sup> and Na<sup>+</sup> ion assembled materials show comparative results, each demonstrating capacities of 56 mAh g<sup>-1</sup> at a 200 mA g<sup>-1</sup> specific current, respectively (i.e., 60% and 57% retention from their initial capacities). This result is likely due to the stated interplay between the interlayer spacing and the improved ion diffusion when the assembling cation is the same as the charge carrying ion. Overall, these two factors play a significant role in determining the mechanism of charge storage, the diffusion coefficient of the charge carrying ions, the cycling stability, and rate capability of Li-LVO/rGO, Na-LVO/rGO, and K-LVO/rGO heterostructures in Li-ion and Na-ion half-cells.

#### 4. Conclusions

This work used Li<sup>+</sup>, Na<sup>+</sup>, and K<sup>+</sup> ions to form a variety of 2D LVO/rGO heterostructures and establish relationships between the final structure and its electrochemical properties. This 'top-down' cation-driven heterostructure assembly approach can be used to define the interlayer spacing of the bilayered vanadium oxide phase by changing the nature of the assembling cation. In turn, the CV curves and galvanostatic cycling highlight the benefit of using an active material with a large interlayer spacing for improved initial capacities. Further, the cations used to assemble the heterostructures can define intercalation sites for charge carrying ions and improve ion diffusion kinetics when the assembling cation and charge carrying ion are identical, as suggested by the charge storage mechanism analysis, GITT, and rate performance testing. However, galvanostatic testing also signifies that crystallographic water can negatively impact the cycling stability.

Cation-driven assembly was also shown to disperse rGO nanoflakes throughout the  $\delta$ -V<sub>2</sub>O<sub>5</sub>·nH<sub>2</sub>O bilayers. STEM analysis found a V<sub>2</sub>O<sub>3</sub> interface that forms along the rGO surface, and galvanostatic testing suggests this feature may help stabilize the heterostructure during electrochemical cycling. In total, these results indicate that an ideal heterostructure consists of a well dispersed electronically conductive phase to tune the stable interface formed between the active material and electronically conductive phase and a 2D active phase with a large interlayer spacing, low water content, and preintercalated cations that are conducive with the chosen charge carrying ions. This theory can be applied to any 'top-down' heterostructure synthesis utilizing 2D materials beyond  $\delta$ -V<sub>2</sub>O<sub>5</sub>·nH<sub>2</sub>O and rGO.

## **Supporting Information**

Cross-sectional SEM images, EDS mapping, and the respective EDS spectra of the M-LVO/rGO (M = Li, Na, K) heterostructures; high-resolution STEM and EELS characterization of the M-LVO/rGO (M = Li, Na, K) heterostructures; XPS survey spectra, XPS spectra of the C1s region, and XPS spectra of the V2p region of (r)GO and M-LVO/(r)GO (M = Li, Na, K) heterostructures and a Table summarizing the binding energies and atomic percentage of each of the respective functional groups; CV curves of the M-LVO-rGO (M = Li, Na, K) electrodes in Li-ion and Naion cells at increasing scan rates, Tables summarizing the diffusion limited and non-diffusion limited capacities of each heterostructure at each scan rate, and representative plots showing how

the diffusion coefficient of Li<sup>+</sup> and Na<sup>+</sup> ions were calculated in their respective charge storage systems; initial discharge/charge voltage profiles of the M-LVO/rGO (M = Li, Na, K) heterostructures in Li-ion and Na-ion cells.

## Acknowledgements

This work was supported by the National Science Foundation (NSF) under Grant No. DMR-1752623. We thank Drexel's Materials Characterization Core (MCC) facility for providing access to characterization instruments. STEM and EELS research was supported by the Center for Nanophase Materials Sciences (CNMS), which is a US Department of Energy, Office of Science User Facility at Oak Ridge National Laboratory.

#### References

- (1) Nitta, N.; Wu, F.; Lee, J. T.; Yushin, G. Li-Ion Battery Materials: Present and Future. *Materials Today* **2015**, *18* (5), 252-264. DOI: 10.1016/j.mattod.2014.10.040.
- (2) Armand, M.; Tarascon, J. M. Building Better Batteries. *Nature* **2008**, *451* (7179), 652-657. DOI: 10.1038/451652a.
- (3) Xu, B.; Qian, D.; Wang, Z.; Meng, Y. S. Recent Progress in Cathode Materials Research for Advanced Lithium Ion Batteries. *Materials Science and Engineering: R: Reports* **2012**, *73* (5-6), 51-65. DOI: 10.1016/j.mser.2012.05.003.
- (4) Zubi, G.; Dufo-López, R.; Carvalho, M.; Pasaoglu, G. The Lithium-Ion Battery: State of the Art and Future Perspectives. *Renewable and Sustainable Energy Reviews* **2018**, *89*, 292-308.
- (5) Zhu, L.; Li, Y.; Zhao, J.; Liu, J.; Wang, L.; Lei, J. Recent Advanced Development of Stabilizing Sodium Metal Anodes. *Green Energy & Environment* **2022**. DOI: 10.1016/j.gee.2022.06.010.
- (6) Liu, S.; Kang, L.; Henzie, J.; Zhang, J.; Ha, J.; Amin, M. A.; Hossain, M. S. A.; Jun, S. C.; Yamauchi, Y. Recent Advances and Perspectives of Battery-Type Anode Materials for Potassium Ion Storage. *ACS Nano* **2021**, *15* (12), 18931-18973. DOI: 10.1021/acsnano.1c08428. (7) Ponrouch, A.; Monti, D.; Boschin, A.; Steen, B.; Johansson, P.; Palacín, M. R. Non-Aqueous
- Electrolytes for Sodium-Ion Batteries. *Journal of Materials Chemistry A* **2015**, *3* (1), 22-42. DOI: 10.1039/c4ta04428b.
- (8) Mineral Commodity Summaries 2023; 2023. DOI: 10.3133/mcs2023.
- (9) Larcher, D.; Tarascon, J.-M. Towards Greener and More Sustainable Batteries for Electrical Energy Storage. *Nature Chemistry* **2015**, *7* (1), 19-29.
- (10) Olivetti, E. A.; Ceder, G.; Gaustad, G. G.; Fu, X. Lithium-Ion Battery Supply Chain Considerations: Analysis of Potential Bottlenecks in Critical Metals. *Joule* **2017**, *1* (2), 229-243.
- (11) Tian, Y.; Zeng, G.; Rutt, A.; Shi, T.; Kim, H.; Wang, J.; Koettgen, J.; Sun, Y.; Ouyang, B.; Chen, T.; Lun, Z.; Rong, Z.; Persson, K.; Ceder, G. Promises and Challenges of Next-Generation "Beyond Li-ion" Batteries for Electric Vehicles and Grid Decarbonization. *Chemical Reviews* **2021**, *121* (3), 1623-1669. DOI: 10.1021/acs.chemrev.0c00767.
- (12) Kim, H.; Ji, H.; Wang, J.; Ceder, G. Next-Generation Cathode Materials for Non-aqueous Potassium-Ion Batteries. *Trends in Chemistry* **2019**, *1* (7), 682-692. DOI: 10.1016/j.trechm.2019.04.007.
- (13) Billaud, J.; Singh, G.; Armstrong, A. R.; Gonzalo, E.; Roddatis, V.; Armand, M.; Rojo, T.; Bruce, P. G.  $Na_{0.67}Mn_{1-x}Mg_xO_2$  ( $0 \le x \le 0.2$ ): a High Capacity Cathode for Sodium-Ion Batteries. *Energy & Environmental Science* **2014**, *7* (4), 1387-1391. DOI: 10.1039/c4ee00465e. (14) Chernova, N. A.; Roppolo, M.; Dillon, A. C.; Whittingham, M. S. Layered Vanadium and Molybdenum Oxides: Batteries and Electrochromics. *Journal of Materials Chemistry* **2009**, *19* (17), 2526. DOI: 10.1039/b819629j.
- (15) Xu, X.; Xiong, F.; Meng, J.; Wang, X.; Niu, C.; An, Q.; Mai, L. Vanadium-Based Nanomaterials: A Promising Family for Emerging Metal-Ion Batteries. *Advanced Functional Materials* **2020**, *30* (10), 1904398. DOI: 10.1002/adfm.201904398.
- (16) Yao, J.; Li, Y.; Massé, R. C.; Uchaker, E.; Cao, G. Revitalized Interest in Vanadium Pentoxide as Cathode Material for Lithium-Ion Batteries and Beyond. *Energy Storage Materials* **2018**, *11*, 205-259.
- (17) Petkov, V.; Trikalitis, P. N.; Bozin, E. S.; Billinge, S. J. L.; Vogt, T.; Kanatzidis, M. G. Structure of V<sub>2</sub>O<sub>5</sub>·nH2O Xerogel Solved by the Atomic Pair Distribution Function Technique.

- *Journal of the American Chemical Society* **2002**, *124* (34), 10157-10162. DOI: 10.1021/ja026143y.
- (18) Clites, M.; Pomerantseva, E. Bilayered Vanadium Oxides by Chemical Pre-Intercalation of Alkali and Alkali-Earth Ions as Battery Electrodes. *Energy Storage Materials* **2018**, *11*, 30-37. DOI: 10.1016/j.ensm.2017.09.005.
- (19) Pomerantseva, E. Chemical Preintercalation Synthesis of Versatile Electrode Materials for Electrochemical Energy Storage. *Accounts of Chemical Research* **2023**, *56* (1), 13-24. DOI: 10.1021/acs.accounts.2c00193.
- (20) Moretti, A.; Maroni, F.; Osada, I.; Nobili, F.; Passerini, S. V<sub>2</sub>O<sub>5</sub> Aerogel as a Versatile Cathode Material for Lithium and Sodium Batteries. *ChemElectroChem* **2015**, *2* (4), 529-537. DOI: 10.1002/celc.201402394.
- (21) Pomerantseva, E.; Gogotsi, Y. Two-Dimensional Heterostructures for Energy Storage. *Nature Energy* **2017**, *2* (7), 17089.
- (22) Liu, Q.; Li, Z.-F.; Liu, Y.; Zhang, H.; Ren, Y.; Sun, C.-J.; Lu, W.; Zhou, Y.; Stanciu, L.; Stach, E. A.; Xie, J. Graphene-Modified Nanostructured Vanadium Pentoxide Hybrids with Extraordinary Electrochemical Performance for Li-ion Batteries. *Nature Communications* **2015**, *6*, 6127. DOI: 10.1038/ncomms7127.
- (23) Clites, M.; Andris, R.; Cullen, D. A.; More, K. L.; Pomerantseva, E. Improving Electronic Conductivity of Layered Oxides through the Formation of Two-Dimensional Heterointerface for Intercalation Batteries. *ACS Applied Energy Materials* **2020**. DOI: 10.1021/acsaem.0c00274.
- (24) Averianov, T.; Pomerantseva, E. Composite Li-ion Battery Cathodes Formed via Integration of Carbon Nanotubes or Graphene Nanoplatelets into Chemical Preintercalation Synthesis of Bilayered Vanadium Oxides. *Journal of Alloys and Compounds* **2022**, *903*, 163929.
- (25) Andris, R.; Averianov, T.; Pomerantseva, E. Phase Transformation and Electrochemical Charge Storage Properties of Vanadium Oxide/Carbon Composite Electrodes Synthesized via Integration with Dopamine. *Journal of the American Ceramic Society* **2022**. DOI: 10.1111/jace.18502.
- (26) Miremadi, B. K.; Morrison, S. R. Preparation of Alternating MoS<sub>2</sub> and WS<sub>2</sub> Single Layers to Form a New MoWS<sub>4</sub> Structure. *Journal of Applied Physics* **1990**, *67* (3), 1515-1520. DOI: 10.1063/1.345661.
- (27) Song, M.-S.; Lee, K. M.; Lee, Y. R.; Kim, I. Y.; Kim, T. W.; Gunjakar, J. L.; Hwang, S.-J. Porously Assembled 2D Nanosheets of Alkali Metal Manganese Oxides with Highly Reversible Pseudocapacitance Behaviors. *The Journal of Physical Chemistry C* **2010**, *114* (50), 22134-22140. DOI: 10.1021/jp108969s.
- (28) VahidMohammadi, A.; Liang, W.; Mojtabavi, M.; Wanunu, M.; Beidaghi, M. 2D Titanium and Vanadium Carbide MXene Heterostructures for Electrochemical Energy Storage. *Energy Storage Materials* **2021**, *41*, 554-562.
- (29) Vahidmohammadi, A.; Mojtabavi, M.; Caffrey, N. M.; Wanunu, M.; Beidaghi, M. Assembling 2D MXenes into Highly Stable Pseudocapacitive Electrodes with High Power and Energy Densities. *Advanced Materials* **2019**, *31* (8), 1806931. DOI: 10.1002/adma.201806931.
- (30) Zhang, R.; Averianov, T.; Andris, R.; Zachman, M. J.; Pomerantseva, E. Liquid Phase Exfoliation of Chemically Prelithiated Bilayered Vanadium Oxide in Aqueous Media for Li-Ion Batteries. *The Journal of Physical Chemistry C* **2023**, *127* (2), 919-929. DOI: 10.1021/acs.jpcc.2c06875.
- (31) Andris, R.; Averianov, T.; Zachman, M. J.; Pomerantseva, E. Cation-Driven Assembly of Bilayered Vanadium Oxide and Graphene Oxide Nanoflakes to Form Two-Dimensional

- Heterostructure Electrodes for Li-Ion Batteries. *ACS Applied Materials & Interfaces* **2023**. DOI: 10.1021/acsami.2c22916.
- (32) Foo, C. Y.; Sumboja, A.; Tan, D. J. H.; Wang, J.; Lee, P. S. Flexible and Highly Scalable V<sub>2</sub>O<sub>5</sub>-rGO Electrodes in an Organic Electrolyte for Supercapacitor Devices. *Advanced Energy Materials* **2014**, *4* (12), 1400236. DOI: 10.1002/aenm.201400236.
- (33) Ramakrishnan, K.; Nithya, C.; Kundoly Purushothaman, B.; Kumar, N.; Gopukumar, S. Sb<sub>2</sub>O<sub>4</sub>@rGO Nanocomposite Anode for High Performance Sodium-Ion Batteries. *ACS Sustainable Chemistry & Engineering* **2017**, *5* (6), 5090-5098. DOI: 10.1021/acssuschemeng.7b00469.
- (34) Li, J.; Huang, J.; Li, J.; Cao, L.; Qi, H.; Cheng, Y.; Xi, Q.; Dang, H. Improved Li-ion Diffusion Process in TiO<sub>2</sub>/rGO Anode for Lithium-ion Battery. *Journal of Alloys and Compounds* **2017**, 727, 998-1005.
- (35) Heising, J.; Kanatzidis, M. G. Exfoliated and Restacked MoS<sub>2</sub> and WS<sub>2</sub>: Ionic or Neutral Species? Encapsulation and Ordering of Hard Electropositive Cations. *Journal of the American Chemical Society* **1999**, *121* (50), 11720-11732. DOI: 10.1021/ja991644d.
- (36) Lu, K.; Hu, Z.; Xiang, Z.; Ma, J.; Song, B.; Zhang, J.; Ma, H. Cation Intercalation in Manganese Oxide Nanosheets: Effects on Lithium and Sodium Storage. *Angewandte Chemie* **2016**, *128* (35), 10604-10608. DOI: 10.1002/ange.201605102.
- (37) BioRender. https://app.biorender.com/ (accessed 2023-03-19).
- (38) Alonso, B.; Livage, J. Synthesis of Vanadium Oxide Gels from Peroxovanadic Acid Solutions: A 51V NMR Study. *Journal of Solid State Chemistry* **1999**, *148* (1), 16-19. DOI: 10.1006/jssc.1999.8283.
- (39) Compton, O. C.; Nguyen, S. T. Graphene Oxide, Highly Reduced Graphene Oxide, and Graphene: Versatile Building Blocks for Carbon-Based Materials. *Small* **2010**, *6* (6), 711-723. DOI: 10.1002/smll.200901934.
- (40) Lu, G.; Ocola, L. E.; Chen, J. Reduced Graphene Oxide for Room-Temperature Gas Sensors. *Nanotechnology* **2009**, *20* (44), 445502.
- (41) Ridley, P.; Gallano, C.; Andris, R.; Shuck, C. E.; Gogotsi, Y.; Pomerantseva, E. MXene-Derived Bilayered Vanadium Oxides with Enhanced Stability in Li-Ion Batteries. *ACS Applied Energy Materials* **2020**, *3* (11), 10892-10901. DOI: 10.1021/acsaem.0c01906.
- (42) Clites, M.; Hart, J. L.; Taheri, M. L.; Pomerantseva, E. Chemically Preintercalated Bilayered K<sub>x</sub>V<sub>2</sub>O<sub>5</sub>·*n*H<sub>2</sub>O Nanobelts as a High-Performing Cathode Material for K-Ion Batteries. *ACS Energy Letters* **2018**, 562-567. DOI: 10.1021/acsenergylett.7b01278.
- (43) Fan, Y.; Qu, Z.; Zhong, W.; Hu, Z.; Younus, H. A.; Yang, C.; Wang, X.; Zhang, S. Understanding the Effect of Interplanar Space and Preintercalated Cations of Vanadate Cathode Materials on Potassium-Ion Battery Performance. *ACS Applied Materials & Interfaces* **2021**, *13* (6), 7377-7388. DOI: 10.1021/acsami.0c23152.
- (44) Feng, H.; Cheng, R.; Zhao, X.; Duan, X.; Li, J. A Low-Temperature Method to Produce Highly Reduced Graphene Oxide. *Nature Communications* **2013**, *4* (1), 1539. DOI: 10.1038/ncomms2555.
- (45) Lipatov, A.; Guinel, M. J. F.; Muratov, D. S.; Vanyushin, V. O.; Wilson, P. M.; Kolmakov, A.; Sinitskii, A. Low-Temperature Thermal Reduction of Graphene Oxide: *In situ* Correlative Structural, Thermal Desorption, and Electrical Transport Measurements. *Applied Physics Letters* **2018**, *112* (5), 053103. DOI: 10.1063/1.4996337.
- (46) Clites, M.; Hart, J. L.; Taheri, M. L.; Pomerantseva, E. Annealing-Assisted Enhancement of Electrochemical Stability of Na-Preintercalated Bilayered Vanadium Oxide Electrodes in Na-Ion

- Batteries. *ACS Applied Energy Materials* **2020**, *3* (1), 1063-1075. DOI: 10.1021/acsaem.9b02098.
- (47) Mansour, A.; Dallek, S.; Smith, P.; Baker, W. Thermogravimetry and X-Ray Absorption Spectroscopy Study of Heated V<sub>2</sub>O<sub>5</sub>·*n*H<sub>2</sub>O Aerogels and Ambigels. *Journal of The Electrochemical Society* **2002**, *149* (12), A1589.
- (48) Wu, Q.-H.; Thissen, A.; Jaegermann, W.; Liu, M. Photoelectron Spectroscopy Study of Oxygen Vacancy on Vanadium Oxides Surface. *Applied Surface Science* **2004**, *236* (1-4), 473-478.
- (49) Kalavathi, S.; Amirthapandian, S.; Chandra, S.; Sahu, P. C.; Sahu, H. Valence State, Hybridization and Electronic Band Structure in the Charge Ordered AlV<sub>2</sub>O<sub>4</sub>. *Journal of Physics: Condensed Matter* **2013**, *26* (1), 015601.
- (50) Wang, J.; Polleux, J.; Lim, J.; Dunn, B. Pseudocapacitive Contributions to Electrochemical Energy Storage in TiO<sub>2</sub> (Anatase) Nanoparticles. *The Journal of Physical Chemistry C* **2007**, *111* (40), 14925-14931. DOI: 10.1021/jp074464w.
- (51) Weppner, W.; Huggins, R. A. Determination of the Kinetic Parameters of Mixed-Conducting Electrodes and Application to the System Li<sub>3</sub>Sb. *Journal of The Electrochemical Society* **1977**, *124*, 1569-1578.
- (52) Amin, R.; Chiang, Y.-M. Characterization of Electronic and Ionic Transport in Li<sub>1-x</sub>Ni<sub>0.33</sub>Mn<sub>0.33</sub>Co<sub>0.33</sub>O<sub>2</sub> (NMC<sub>333</sub>) and Li<sub>1-x</sub>Ni<sub>0.50</sub>Mn<sub>0.20</sub>Co<sub>0.30</sub> (NMC<sub>523</sub>) as a Function of Li Content. *Journal of The Electrochemical Society* **2016**, *163* (8), A1512-A1517. DOI: 10.1149/2.0131608jes.
- (53) Byles, B. W.; Pomerantseva, E. Effect of 1D Diffusion Channel Size and Ionic Content on Li<sup>+</sup> ion and Na<sup>+</sup> ion Diffusion in Tunnel Manganese Oxides. *Materialia* **2021**, *15*, 101013.
- (54) Gao, Q.; Sun, W.; Ilani-Kashkouli, P.; Tselev, A.; Kent, P. R. C.; Kabengi, N.; Naguib, M.; Alhabeb, M.; Tsai, W.-Y.; Baddorf, A. P.; Huang, J.; Jesse, S.; Gogotsi, Y.; Balke, N. Tracking Ion Intercalation into Layered Ti<sub>3</sub>C<sub>2</sub> MXene Films Across Length Scales. *Energy & Environmental Science* **2020**, *13* (8), 2549-2558. DOI: 10.1039/d0ee01580f.
- (55) Wangoh, L. W.; Huang, Y.; Jezorek, R. L.; Kehoe, A. B.; Watson, G. W.; Omenya, F.; Quackenbush, N. F.; Chernova, N. A.; Whittingham, M. S.; Piper, L. F. J. Correlating Lithium Hydroxyl Accumulation with Capacity Retention in V<sub>2</sub>O<sub>5</sub> Aerogel Cathodes. *ACS Applied Materials & Interfaces* **2016**, 8 (18), 11532-11538. DOI: 10.1021/acsami.6b02759.
- (56) Muthukumar, K.; Rajendran, S.; Sekar, A.; Chen, Y.; Li, J. Synthesis of V<sub>2</sub>O<sub>5</sub> Nanoribbon–Reduced Graphene Oxide Hybrids as Stable Aqueous Zinc-Ion Battery Cathodes via Divalent Transition Metal Cation-Mediated Coprecipitation. *ACS Sustainable Chemistry & Engineering* **2023**, *11* (6), 2670-2679. DOI: 10.1021/acssuschemeng.2c07629.

# **Table Of Contents Graphic**

